PHILOSOPHICAL TRANSACTIONS A

The effect of rock particles and D_2O replacement on the flow behaviour of ice

Journal:	*Philosophical Transactions A*
Manuscript ID	RSTA-2015-0349.R1
Article Type:	Research
Date Submitted by the Author:	n/a
Complete List of Authors:	Middleton, Ceri; Universite Libre de Bruxelles, Laboratoire de Glaciologie; Universite Libre de Bruxelles, Non-linear Physical Chemistry Unit Grindrod, Peter; Birkbeck University of London, Department of Earth and Planetary Sciences Sammonds, Peter; University College London, Earth Sciences
Issue Code: Click here to find the code for your issue.:	ICE
Subject:	Glaciology < EARTH SCIENCES
Keywords:	ice-rock rheology, triaxial deformation, D₂O-ice-rock rheology, ice-rock flow laws

PHILOSOPHICAL TRANSACTIONS A

Phil. Trans. R. Soc. A.
doi:10.1098/not yet assigned

The effect of rock particles and D_2O replacement on the flow behaviour of ice

Ceri A. Middleton[1,2,3,4], Peter M. Grindrod[3,5] and Peter R. Sammonds[4]

*[1]Now at: Laboratoire de Glaciologie, Université libre de Bruxelles (ULB), CP 160/03, 50 Avenue F.D. Roosevelt, B-1050 Brussels, Belgium, (*ceri.middleton@ulb.ac.be). [2]Now at: Non Linear Physical Chemistry Unit, Université libre de Bruxelles (ULB), Boulevard du Triomphe, B-1050, Brussels, Belgium [3]Centre for Planetary Sciences at UCL/Birkbeck, Gower Street, London, WC1E 6BT, U. K. [4]Department of Earth Sciences, UCL, Gower Street, London, WC1E 6BT, U.K. [5]Department of Earth and Planetary Sciences, Birkbeck, University of London, Malet Street, Bloomsbury, London, WC1E 7HX, U.K.*

Keywords: ice-rock rheology; triaxial deformation; D_2O-ice-rock rheology; ice-rock flow laws

Summary

Ice-rock mixtures are found in a range of natural terrestrial and planetary environments. To understand how flow processes occur in these environments, laboratory derived properties can be extrapolated to natural conditions through flow laws. Here, deformation experiments have been carried out on polycrystalline samples of pure ice, ice-rock and D_2O-ice-rock mixtures at temperature = 263, 253 and 233 K, confining pressure = 0 and 48 MPa, rock fraction = 0 – 50 vol.%, and strain-rate = 5 x 10^{-7} - 5 x 10^{-5} s^{-1}. Both the presence of rock particles and replacement of H_2O by D_2O increase bulk strength. Calculated flow law parameters for ice and H_2O-ice-rock are similar to literature values at equivalent conditions, except for the value of the rock fraction exponent, here found to be 1. D_2O samples are 1.8 times stronger than H_2O samples, likely due to the higher mass of deuterons when compared to protons. A gradual transition between dislocation creep and grain-size-sensitive deformation at the lowest strain-rates in ice and ice-rock samples is suggested. These results demonstrate that flow laws can be found to describe ice-rock behaviour, and should be used in modelling of natural processes, but that further work is required to constrain parameters and mechanisms for the observed strength enhancement.

1. Introduction

Icy environments in both terrestrial and planetary settings rarely consist of pure H_2O-ice, but often contain an intimate mixture of ice and other material, including silicates. These mixtures are found in settings as diverse as frozen soil and permafrost environments on both the Earth [1] and other planets [2,3], at the base of terrestrial ice sheets and glaciers [4–6], and in the interiors of outer solar system icy planetary bodies [7,8]. When considering flow processes that occur in these environments, rheological properties are determined in controlled laboratory experiments, and then extrapolated to conditions found in nature using flow laws. However, the rheological behaviour of ice-rock mixtures at a range of conditions and rock fractions is not fully explored in the literature [6,9]. Using different rheologies in models of icy moon evolution leads to first-order differences in the internal structure (e.g. [10]). Therefore it is important to understand the individual factors that control this rheology, allowing tighter constraints on simulated behaviour.

Previous studies into the properties of pure water ice at a range of conditions have allowed deformation mechanisms to be identified, and flow laws to be calculated, of a form similar to:

$$\dot{\varepsilon} = A\sigma^n exp\left(\frac{-(Q + PV^*)}{RT}\right) \quad \text{(Eq. 1)}$$

*Author for correspondence (ceri.middleton@ulb.ac.be).
†Present address: Laboratoire de Glaciologie, Université libre de Bruxelles (ULB), CP 160/03, 50 Avenue F.D. Roosevelt, B-1050 Brussels, Belgium

where $\dot{\varepsilon}$ is the strain-rate, σ is the steady-state stress, P is confining pressure, V* is the activation volume, R is the gas constant and T is the temperature, and the flow law parameters A, n, and Q (activation energy) are defined experimentally for each deformation mechanism [6,11–13].

The effect of particulate matter on this behaviour at high homologous temperatures has been shown to be important during deformation of frozen soils: the early stages of deformation are influenced by the presence of ice, but further strain results in increased strength due to contact and friction between rock particles [1,14–19]. At colder temperatures, studies with no imposed confining pressure have also shown an increase in strength with increasing rock fraction above a critical rock fraction of 10-15 vol.%. Below this rock fraction, the behaviour is similar to pure ice [4,20]. However, the unconfined conditions in these tests may have led to fracture at higher rock fractions [20]. One study that has successfully considered ductile deformation of ice-particulate mixtures at a range of confining pressures, rock fractions, and lower temperatures is that of Durham et al. (1992) [21]. This work found that at a rock volume fraction >10 vol.%, strength increased, and at 56 % the strength was close to that of the dry sand material. This increased strength was suggested to be due to viscous drag in the ice as it flowed around the hard particulates. From this data, a flow law for the behaviour of ice-rock mixtures has been suggested:

$$\sigma_{ice-rock}(P,T,\dot{\varepsilon}) = \sigma_{pure\ ice}(P,T,\dot{\varepsilon}) \times e^{b\varphi_{rock}} \quad \text{(Eq. 2)}$$

where σ is the steady-state stress, $\dot{\varepsilon}$ is the the steady-state strain-rate, φ_{rock} is rock volume fraction, and b is a dimensionless parameter, found to be ~2 [22]. It is important to note, however, that the particle size and composition of the rock was not consistent between the different rock volume fractions, which may have an effect on the measured rheology, and that it is important for experimentally defined flow laws to be independently verified.

D_2O-ice is used as a replacement for H_2O in experiments carried out in neutron beamlines e.g. [23–27], where replacement of H_2O by D_2O is necessary to avoid incoherent scattering of the diffracted beam [28,29]. These *in situ* studies have allowed the evolution of texture during deformation to be observed, and grain scale changes linked to the dominant deformation mechanism to be identified [26]. This study has shown that the detailed deformation behaviour of H_2O (deformed at 263 K) and D_2O (deformed at 266 K) is similar, however the peak stress of D_2O is higher than the peak stress of the H_2O sample. These results have been taken as confirmation that H_2O and D_2O behave the same during deformation [25,27], although this supposition seems to neglect the fact that the peak stress is higher for the D_2O sample. Wilson et al. [26] also show data for a D_2O-ice+calcite experiment which demonstrates similar gross behaviour, with additional strain hardening at high total strains, with no apparent increase of peak stress when compared to the pure D_2O ice sample deformed at the same conditions. However, the calcite volume fraction is not given, so may be below the critical rock fraction (10-15 vol.%) mentioned above, and so peak stress and steady state stress may be expected to be the same as the pure D_2O ice situation. In another study, it was found that the mechanical relaxation time of D_2O-ice is higher by a factor of 1.5 when compared to H_2O-ice [28], due to the different masses of deuterons and protons.

Here, we add to the available experimental data on the properties of ice-rock materials and D_2O ice by carrying out deformation experiments on ice, ice-rock and D_2O-ice-rock samples at a range of conditions. The methodology is described in Section 2, including sample preparation, deformation procedure and microstructural analysis. Results of these experiments are presented in Section 3. A discussion of these results, with empirical flow laws that include the effect of a rock component and the replacement of H_2O by D_2O, is shown in Section 4, where potential mechanisms for strength enhancement mechanism are also discussed. A summary of the conclusions and recommendations for future work is presented in Section 5.

2. Method

2.1 Sample manufacture

Polycrystalline right-circular cylindrical pure ice, H_2O-ice-rock and D_2O-ice-rock samples were produced using a variation of the seed methods used previously [20,30,31]. These samples conformed to certain criteria required to collect reliable rheological information: a sample length that is 2.5-3 times that of the diameter, a grain size small enough to allow at least 10 grains across the diameter of the sample, a homogeneous distribution of the constituent materials, with randomly oriented grains [6,32–35]. Samples had a nominal diameter 25 mm, length 65 mm, and grains of size 125-500 µm. The nominal rock volume fraction for H_2O-ice-rock and D_2O-ice-rock samples was controlled to 10, 25 and 50 vol.% by adjusting the ratio of ice to rock seeds. The methodology differed depending on the rock volume required, so these methodologies will be described separately. Examples of pre-deformation microstructures can be seen in Figure 1, details of the procedure for obtaining these images are given in Section 2.3.

2.1.1 Pure water ice samples

Ice seeds were produced from deionised water, firstly degassed by boiling, then cooled under its own vacuum and frozen at 253 K. This ice was crushed using a commercial ice crushing machine, ground to a fine powder using a coffee grinder and sieved to the required 100-200 μm seed size. A small amount of deaerated water cooled to 273 K was introduced to a cylindrical mould of 25 mm diameter, then a small amount of ice seeds at the same temperature were introduced slowly whilst stirring. This process was repeated until the length of sample required was reached, then the samples were frozen overnight at 253 K where ice seeds acted as nucleation points for randomly oriented crystal growth. After freezing, samples were removed from the moulds by gentle warming of the moulds by the hands, allowing a thin melt layer to lubricate their movement. Samples were machined to the size required, with flat parallel faces (within 0.1 mm), using a lathe. No preferred orientation of ice crystals was found using an Automatic Ice Fabric Analyser [36] or in microstructural analysis of samples, using optical and scanning electron microscopy (Figure 1). Sample preparation was carried out in a cold room at a temperature of 263 K in the UCL Ice Physics laboratory.

The porosity of the samples ($\varphi_{porosity}$) was calculated using:

$$\varphi_{porosity} = \left(1 - \frac{V_{ice}}{V_{total}}\right) = \left(1 - \frac{M_{total}/\rho_{ice}}{V_{total}}\right) \quad \text{(Eq. 3)}$$

where V_{ice} is the calculated volume of the ice, V_{total} is the total measured volume of the sample, M_{total} is the measured total mass of the sample, ρ_{ice} is the density of the ice (917 kg m^{-3} [37]). The porosities of the pure ice samples were all on the order of 2 ± 1 vol.%, (full sample details in Table 1).

2.1.2 Ice-rock samples

Fluorite (CaF_2) was chosen as the "rock" component, to allow comparison with a companion experiment carried out in a neutron diffraction facility [38]. The use of a "non-natural" rock component involves the assumption that the composition of the rock is not important, and that the rock particles are behaving as inert particles within a matrix of ice. Also, microstructural observations show that the fluorite particles are angular (Fig. 1), and are therefore distinct from particles which have been eroded during transport, which may affect how deformation occurs. Fluorite was crushed to ~1 cm in size, ground with a disk mill, and then sieved to the desired particle size (100-200 μm). For ice-rock samples of 10 and 25 vol.%, ice seeds and rock particles were combined at ratios calculated to result in the required rock fractions, before being carefully mixed with the deaerated, deionised water. This procedure involved adding a small amount of liquid water to the mould, then introducing a small amount of ice and rock seeds whilst stirring, then repeating, similar to the method of Yasui and Arakawa [20]. This gradual introduction of ice and rock seeds was necessary to stop the denser fluorite particles sinking and less dense ice particles floating. For the highest rock fraction samples, no ice seeds were added to the mould, rather, rock particles were added directly to the deaerated water.

After freezing and machining, the final rock volume fractions (φ_{rock}) were calculated:

$$\varphi_{rock} = \left(1 - \varphi_{porosity}\right)\left(\frac{\frac{\rho_{avg}}{(1-\varphi_{porosity})} - \rho_{ice}}{\rho_{rock} - \rho_{ice}}\right) \quad \text{(Eq. 4)}$$

where $\varphi_{porosity}$ = volume of porosity (assumed to be the same as calculated for pure ice samples = 2 %), $\rho_{avg} = M_{total}/V_{total}$, ρ_{rock} is the density of the fluorite (3180 kg m^{-3} [39]).

2.1.3 D_2O ice-rock samples

The manufacture of D_2O ice-rock samples was as above, with care taken to avoid contamination of the D_2O by substitution with H_2O in the air; liquid D_2O was kept in sealed containers at all times. During deaeration of the D_2O by boiling, the steam was bubbled through a small amount of D_2O to avoid interactions with, and contamination by, atmospheric water. D_2O-ice seeds were produced in the same way as H_2O-ice seeds, with care taken to clean the apparatus and sieves of all H_2O beforehand. Seeds were then mixed with fluorite particles and cooled liquid D_2O in the same way as H_2O-ice-rock samples for the 10 and 25 vol.% fluorite samples. 50 vol.% fluorite samples were produced from flooding fluorite particles with liquid D_2O. The rock volume fractions of the D_2O samples were calculated using Eq. 4, replacing the density of H_2O ice with that of D_2O ice (1019 kgm^{-3}, calculated from the lattice parameters of [40] at 250 K).

2.2 Deformation

Ductile deformation experiments on H_2O-ice, H_2O-ice-rock mixtures, and some D_2O-ice-rock mixtures were carried out in the digital servo-controlled, electro-mechanical triaxial ice deformation rig in the UCL Rock and Ice Physics Laboratory, designed to function at strain rates between 2 x 10^{-9} and 1 x 10^{-2} s^{-1}. Full details, schematics and calibration

information of this apparatus can be found in Sammonds et al, and Rist et al. [41,42]. This apparatus uses nitrogen gas as a confining medium, with an additional stress applied along the axe of the sample, such that $\sigma_1 > \sigma_2 = \sigma_3$. Deformation of some D_2O-ice-rock samples was also carried out on the Engin-X beamline at the ISIS neutron spallation facility, using a custom built pressure vessel to provide confining pressure, and the in-house 100 kN Instron stress rig to provide differential stress [38]. Experiments at both locations were carried out at a nominal confining pressure of 48 MPa, and temperatures of 263, 253 and 233 K. Three ambient pressure runs at 263 K were also carried out in the UCL deformation rig. A differential stress was applied at a nominally constant strain-rate between 5×10^{-7} and 5×10^{-5} s^{-1}, (in reality a constant displacement rate), and the stresses reached were measured with inbuilt load cells. Strain-rate ramping was used to increase the amount of data retrieved from some samples. Data were corrected for the deformation in the load chain with reference to a sample of known properties, for the change in sample length by calculating a revised strain-rate based on the sample length at a given time, and for the effect of seal friction and overcoming confining pressure by normalising the data to a zero-point as contact was made on the sample [42,43].

2.3 Microstructural analysis

Microstructural analysis of the textures before and after deformation was carried out using both traditional light microscopy (in transmitted and reflected light), with an Olympus Vanox-T microscope, and scanning electron microscopy using a JEOL JSM-6408LV Scanning Electron Microscope (SEM) with a Gatan CT1500 cryostage attachment. Pre-deformation samples were purposefully produced at longer lengths than necessary for the deformation, so that during machining, sections could be removed for microstructural analysis. Sections were taken from the central areas of deformed samples, both parallel and perpendicular to the direction of maximum stress.

Pure ice sections for light microscopy were produced using a microtome [44]. Once polished, sections were stored at 253 K overnight to allow sublimation etching, which occurs preferentially at grain boundaries [13,28]. Ice-rock sections were polished by hand with sand paper of decreasing grit sizes, as the fluorite component was too stiff to be cut with the microtome blade. This resulted in thicker, less polished sections than for pure ice samples. SEM samples were formed by sawing small chips of sample and freezing them into a welled stub (8 mm in diameter). Once the sample was mounted in the SEM, the stage was heated very briefly to 190 K to sublimate frost, enhance grain boundary grooves [13,28,45] and etch the surface, which allowed determination of the crystal orientation [28,46]. After sublimation, observations were carried out at 88 K.

Example microstructures can be seen in Figure 1, where pure ice samples show grains of a similar size, with a hexagonal ice grain habit (Figure 1a-c). Porosity is seen as small air pockets at intersections of grain boundaries, particularly at triple junctions (Figure 1a). Quasi-parallel grooves within individual ice grains (indicated by arrows in Figure 1c) are due to sublimation etching. This linear sublimation texture is oriented differently in adjacent grains, demonstrating the random orientation of grains. Ice-rock samples show angular fluorite particles in a matrix of ice (Figure 1d-f), the fluorite grains have been colourised purple in post-processing to highlight their position. Within this matrix, hexagonal ice grain boundaries can again be seen, except for at the highest rock fraction (Figure 1f). Sublimation pitting can be seen in Figure 1e. The shape and orientation of these pits is determined by the orientation of the ice crystal [28,46], so as the etch pits in adjacent grains are oriented differently, we can suggest that the grains are also oriented differently.

Line-intercept analysis [47] of thin section and SEM images shows an ice grain size of 360 ± 120 µm (1 s.d.), with a range from 125-500 µm for pure ice samples, with ice-rock samples of intermediate rock fraction showing a lower average of 185 ± 50 µm (1 s.d.) with a range of 125-300 µm. Ice grain boundaries are not visible in the highest rock fraction samples, so we are unable to determine if the ice grain size differs in those samples.

3. Results

Details of each sample produced, and deformation conditions for each experimental run are shown in Table 1, along with the measured steady-state stresses recorded at the imposed strain-rates for each experimental run. An example of one experimental run is shown in Figure 2, where strain and stress over the course of deformation of one ice + 50 vol.% sample are plotted as a function of time. Details of the deformation behaviour are highlighted: seal friction, before contact is made on the sample (A), the point where deformation begins (B), transient creep (C). The plateau where stress no longer increases is steady-state creep, the average of which is the value reported in Table 1 (D). Strain-rate ramping, which was used on most samples, can be seen at points (E) and (F), where the gradient of the strain curve increases, accompanied by an instant increase in the stress values before levelling to a further steady-state plateau. Strain hardening

behaviour, where stress continues to increase with increased strain can be potentially seen in the second strain-rate ramp (G), where it is definitely found at the highest recorded strains for the third strain-rate (H). From analysis of other individual stress-strain curves, similar strain hardening occurs at high strains in samples of all rock fractions, in both H_2O and D_2O samples. Strain hardening is also seen at lower strains in 50 vol.% rock samples, prolonging transient creep and delaying the onset of steady-state creep. Strain softening behaviour, where an initial peak stress decreases to a constant steady-state stress, can also be seen in some higher strain-rates experiments for samples of 0, 10 and 25 vol.% rock in both H_2O and D_2O samples.

The measured steady-state stresses for pure ice and H_2O-ice-rock samples deformed at a range of strain-rates, a confining pressure of 48 MPa and a temperature of 253 K are shown in Figure 3. The measured stresses range between 2 and 15 MPa, with higher stresses recorded at higher strain-rates. Samples of 10 vol.% rock register similar stresses to pure ice samples, but above this rock fraction the stress at a given strain-rate increases with increasing rock fraction. The effect of temperature and confining pressure can be seen in Figure 4, where 50 vol.% rock samples deformed at atmospheric conditions register much lower stresses than equivalent confined samples (a factor of 4 difference in strength). Pure ice samples and 50 vol.% samples deformed at 263 K support a lower stress than those deformed at 253 K. D_2O-ice-rock samples also demonstrate an increased stress with increased strain-rate and decreased temperature, as can be seen in Figure 5. The relationship with rock fraction is not as clear as in the H_2O samples, as there is a large range of values for the 25 vol.% rock samples, but it can be seen that there is an increased strength between the 10 vol.% and 50 vol.% samples. The strengths of D_2O samples are higher than equivalent H_2O samples by a factor of ~2, this increase and a suggested mechanism responsible for it will be considered further in Section 4.2.3.

Post-deformation microstructures observed in ice and ice-rock samples are shown in Figure 6. When compared to pre-deformation samples, the pure ice post-deformation microstructure qualitatively shows a larger range of grain size, with features such as recrystallisation, sub-grain development, and grain boundary movement visible (Figure 6a). Previous observations of pure ice have shown similar microstructural textures to those observed here in deformed samples in both natural [48–50] and experimental [51] samples. Similar grain size changes can be seen in the 10 vol.% rock sample in Figure 6b, with smaller ice grains highlighted. Grain boundary bulging and movement can be seen in both Figure 6c and d (10 vol.% rock), the previously straight grain boundaries replaced with curving boundaries. Potential recrystallisation with ice crystals of a more rectangular habit can be seen in Figure 6c and also in the 25 vol.% sample in Figure 6e; in Figure 6e this rectangular grain behaviour may be associated with the central fluorite grain. The sub-grain boundary highlighted in the top right of Figure 6d is potentially linked to the angular fluorite particle that is just inside the field of view, seeming to run along the rock particle and through the ice grain. In the highest rock fraction samples (Figure 6f), the rock particles appear fractured and fragmented, and only a small amount of the surrounding ice matrix can be seen, with no ice grain detail visible.

4. Discussion

4.1 Strain hardening and softening

Analysis of individual stress-strain curves can reveal detail about the processes occurring during deformation. For example, previous studies of pure ice have linked strain hardening at high strains to ice recrystallisation [52]. Here, we observe strain hardening at high strains in both pure ice and ice-rock samples at all rock fractions. The microstructural observations of ice recrystallisation (Figure 6) support this as a mechanism of hardening in ice-rock as well as pure ice. Strain hardening also occurred at lower strains in 50 vol.% rock samples, delaying the onset of steady-state flow when compared to lower rock fractions. Microstructural observations (Figure 6f) suggest contact and fracturing in the fluorite particles, likely due to impaction during deformation. This fracturing supports a similar mechanism to that seen in previous studies, where contact between rock particles caused friction and inhibited flow of the mixture [2,14,20,21].

Another feature seen in some individual stress-strain curves was the presence of strain softening behaviour, where a peak stress was followed by a slight decrease and then levelling to a constant “steady-state” value. This behaviour was not seen in all of the deformation runs in this study, which is in contrast to the previous results of Durham et al. (1992) [21], who observed strain softening in all of their deformation runs on samples of ice and ice-rock. The results of Wilson et al. (2014) [26] also show strain softening in D_2O and D_2O-ice-rock samples. The difference in the presence of strain softening may be due to the different experimental conditions in these studies, therefore variables such as the composition of the rock, temperature, grain-size and rock volume fraction should be investigated more fully in future studies.

4.2 Flow laws and deformation mechanisms

4.2.1 Pure ice

Flow law parameters A, n and Q have been calculated from the measured data for a flow law of the form shown in Equation 1 (Table 2). The value of n = 4, combined with the microstructural observations (Figure 6), are indicative of dynamic recrystallisation by grain boundary migration, a dislocation creep mechanism [13,21,53], which agrees with predictions from the strain-rate, temperature, confining pressure and grain size conditions in this study [11,54]. The value of the activation energy reported here (106.1 ± 16.5 kJ mol^{-1}) is within the bounds of previously reported values for dislocation creep, e.g. 91 kJ mol^{-1} between 240-258 K [21] and 181 kJ mol^{-1} at >258 K [13]. The values of P (48 MPa), R (8.31 J K^{-1} mol^{-1}) and V* (-13 cm^3 mol^{-1}; [21]) are assumed constant.

It is also possible that within the full data set, a gradual transition between two dominant deformation regimes occurs: at the lowest strain-rates (below 1.5 x 10^{-5} s^{-1}), measured stresses were lower than might be expected from the fitted flow law (Figure 4a). This transition may be due to the boundary between dislocation creep and grain-size-sensitive (GSS) deformation [11] being approached, allowing grain size induced weakening [55]. To consider this theory, the data set was separated into "high" strain-rates (above 1.5 x 10^{-6} s^{-1}) and "low" strain-rates (below 1.5 x 10^{-6} s^{-1}), and the flow law parameters recalculated (Table 2, high strain-rate and low strain-rate scenarios). In the high strain-rate regime, n was found to be 5, a higher value than previously reported for ice at these conditions [11] but still indicative of dislocation creep [56].

There are not enough low strain-rate data to fully investigate a flow law in the GSS regime. However as a first approximation, literature values for the grain boundary sliding-accommodated basal slip parameters: Q, n, and p (T < 255K) [13] have been combined with the available low strain-rate data to calculate a value of A in a flow law of the form:

$$\dot{\varepsilon} = A\sigma^n d^{-p} exp\left(\frac{-(Q + PV^*)}{RT}\right) \quad \text{(Eq. 5)}$$

where d is grain size, p is the grain size exponent [13], (values shown in Table 2). Unfortunately, any textural evidence of a lower strain-rate deformation mechanism will have been removed by the strain-rate ramping, so microstructural observations cannot be used here to consider this lower strain-rate mechanism.

Rather than an abrupt change between two straight lines (as shown in Figure 4a), the data here may describe a curve, representing a gradual transition between the two dominant deformation mechanisms, so requiring a combined flow law to fully understand [13]. However, a full consideration of this combined flow law would require further data, either at lower strain-rates, or samples with a smaller grain size at similar strain-rates [13].

4.2.2 Enhancement factor for rock

From the difference in stress measured at 5 x 10^{-5} s^{-1}, an addition of 50 vol.% rock would enhance the effective viscosity compared to pure ice by a factor of 2. This increase in strength due to the inclusion of rock particles can be included in the flow law by introducing an enhancement factor [20]. To find this enhancement factor, the flow strength of the ice-rock mixtures was normalised using the pure ice flow law, to give an adjusted flow stress:

$$\sigma_{adj} = \frac{\sigma_{ice-rock}(measured)}{\sigma_{ice}(calculated)} \quad \text{(Eq. 6)}$$

Any deviation of the adjusted flow stress from the pure ice flow law can then be attributed to the rock component in the sample.

Durham et al. (1997) [22] represented the ice-rock data of Durham et al. (1992) [21] by the flow law shown in Equation 2. Combining Equations 2 and 6, the relationship between the rock fraction and adjusted flow stress (σ_{adj}) becomes:

$$\sigma_{adj} = e^{b\varphi_{rock}} \quad \text{(Eq. 7)}$$

A fit of this equation to the adjusted flow stresses found from Equation 6 results in a value of b ~1 (Table 2). The difference between the value of b found here, and that found previously (b = 2, [11,22]) would equate to a factor of ~1.5 difference in calculated effective viscosity when implemented in the flow law. Possible explanations for the difference could include variations in experimental conditions, rock composition, rock particle size or ratio of rock particle size to ice grain size, but further work is necessary to refine the causes. The previous equations can be rearranged to an ice-rock flow law of the form:

$$\dot{\varepsilon}_{ice-rock} = \left(\frac{\sigma_{ice-rock}}{e^{b\varphi}}\right)^n A\, exp\left(\frac{-(Q + PV^*)}{RT}\right) \quad \text{(Eq. 8)}$$

Calculated ice-rock flow laws are plotted with the measured data in Figure 4b-d, showing a fit with some scatter for both n = 4 and n = 5 scenarios. The microstructural observations of ice + 10 and 25 vol.% rock show similar post-deformation features to those in the pure ice samples: evidence of recrystallization, sub-grain boundary formation, grain boundary bulging and migration. Some of these features appear to be associated with the rock particles, such as the irregular grain boundaries in Figure 6d, and the sub-grain boundaries perpendicular to the ice-rock grain boundary in Figure 6e. The presence of these features suggests that dislocation creep is again the mechanism of deformation in the ice, which corresponds well to a value of n = 4 or 5.

As with pure ice, the lowest strain-rate data for 25 and 50 vol.% may be better represented by a flow law with n = 1.8, suggesting that a change in deformation mechanism occurs in both pure ice and ice-rock samples at similar strain-rates. The inclusion of rock particles does not, therefore, seem to change the deformation mechanism, nor where a transition between dominant mechanisms occurs, but must affect the deformation in another way.

An increased concentration of dislocations around rock particles has previously been suggested as a mechanism for increased strength in ice-rock mixtures [4]. However, Durham et al. 1992 [21] found that the predicted increase in strength from pinning of dislocations was not sufficient to explain the observations in their experiments, and so determined that viscous drag around the rock particles was taking place. Here, the presence of deformation features associated with rock particles suggests that these pinned dislocations are mobilised during deformation, which may in turn impede the flow around the rock particles.

Although discussion of the temperature dependence of the flow law was not the aim of this study, it can be seen in Figure 4 that pure ice data can be well described by the calculated flow laws at the two temperatures. However, flow laws including the effect of a rock component do not well describe the 50 vol.% data at 263 K. A temperature dependence to the data is still present, however, the 263 K flow law underestimates the stress for any given strain-rate. At these temperatures, it is also possible that pre-melting behaviour was present, as has been seen previously in both ice and ice-rock samples with grain boundary wetting enhancing diffusion, and weakening samples [11,13,57]. However, if present, this effect seems to be lower in the ice-rock samples, as the measured strength is higher than anticipated from flow laws deduced from the temperature dependence of pure ice. We suggest that the effect of temperature on the higher rock fraction samples was lessened due to the lower ice fraction and larger contact between rock particles. The effect of confining pressure on the behaviour of ice-rock materials is not considered here, but we can note that the few data points of ice + 50 vol.% rock, at atmospheric pressure, would not be well described by the ice-rock flow law described. However, at conditions with no applied confining pressure, it is possible at these high rock fractions that brittle failure is becoming more important [3,20]. Therefore a combined rock fraction, temperature and confining pressure study would be of interest for future work to fully understand these effects, and the critical rock fractions where they occur.

As stated previously, the choice of fluorite in this study was necessitated by the companion neutron diffraction experiments, but the composition of the rock particles, and the shape of those particles, may influence the rheological behaviour, hence being a constraint on the value of the parameter 'b', so would be an important consideration for further studies.

4.2.3 Enhancement factor for D_2O ice

D_2O-ice-rock samples demonstrate a higher strength than H_2O-ice-rock samples at equivalent strain-rates. Unfortunately D_2O is expensive, so a full rheological study of heavy water ice was not possible within this study, and no pure D_2O-ice samples were deformed. However, a flow law for D_2O ice-rock mixtures and a potential mechanism for the observed difference in strength between H_2O and D_2O ice-rock samples are considered briefly here.

An enhancement factor for D_2O ("k", the value by which the strength of the D_2O ice-rock sample is higher than the strength of an equivalent H_2O-ice-rock sample) was determined using a similar approach to Section 4.2.2:

$$k = \frac{\sigma_{D_2O-ice-rock}(measured)}{\sigma_{H_2O-ice-rock}(calculated)} \quad \text{(Eq. 9)}$$

The calculated mean values of k are 1.80 ± 0.42 for n = 4, or 1.70 ± 0.38 for n = 5. This value of k is independent of rock fraction and strain-rate and can be treated as an independent constant in the flow law:

$$\dot{\varepsilon}_{D_2O-ice-rock} = \left(\frac{\sigma_{D_2O-ice-rock}}{k e^{b\varphi}}\right)^n A \, exp\left(\frac{-(Q + PV^*)}{RT}\right) \quad \text{(Eq. 10)}$$

The calculated flow laws for D_2O (Figure 5) do not fit the measured data as well as the H_2O data. The observed differences may be due to relatively large errors on the calculated value of k, the scarcity of D_2O data points, and the fact that the D_2O experiments were carried out on two different experimental set-ups. Again we can suggest that a GSS deformation mechanism is present at the lowest strain-rate for the 10 vol.% data. Unfortunately, there are currently insufficient data to confirm this, nor deduce whether any change in deformation mechanism occurs in D_2O samples at similar strain-rates to those found in H_2O.

The predicted flow law at 233 K for D_2O-ice + 10 vol.% rock overestimates the measured stress of the single data point at these conditions. Previously we drew the conclusion that for a 50 vol.% rock sample, an underestimation of the stress was due to the lower ice fraction present. However, with a low rock fraction, we would expect a much closer relationship to that of the pure ice. It is, of course, difficult to draw conclusions from one datum, but we suggest that the conditions for this deformation run may have been within a low temperature deformation regime, as seen previously in pure H_2O-ice samples [11]. It may be the case, as mentioned above, that our higher temperature data is present in a regime where pre-melting of ice at grain boundaries is possible, decreasing the strength, due to enhanced grain boundary sliding and diffusion. At 233 K, the lower temperature may inhibit pre-melting, so explaining the higher strength and why a flow law with parameters found at higher homologous temperatures would not be appropriate here.

Under the assumption that rock particles have the same effect in D_2O-samples as H_2O-samples, we can suggest that the increase in strength between H_2O-ice-rock sample and D_2O-ice rock samples is due to the presence of the deuterated water. This assumption is difficult to consider here without results from pure D_2O-ice samples, however as H_2O-ice + 10 vol.% samples show similar behaviour to pure ice (Figure 3), the reverse inference - that pure D_2O ice behaves the same as D_2O-ice + 10 vol.% - seems plausible. We would stress that this assumption should be investigated in future studies. The mechanism suggested previously to explain a difference in mechanical relaxation time between H_2O and D_2O-ice [28], could then also be used to explain the strength difference seen in these deformation experiments. Bjerrum defects are present in the Ice Ih structure due to the position of protons (hydrogen atoms) on the bonds between oxygen atoms, these defects must move before dislocations can progress through the ice lattice during deformation, so requiring rearrangement of the protons [58]. The mass difference between the proton and the deuteron may result in slower rearrangement of the deuterons, inhibiting dislocation movement, and thereby increasing the flow strength.

If this increase in strength is entirely due to the D_2O structure, then the explicit assumption of previous studies, that D_2O samples have the same mechanical properties as H_2O samples, and that differences in deformation behaviour can be normalised by a three degree difference in experimental temperature [25,26], may be overly simplistic, and should be re-examined.

5. Conclusion

This study shows that considerable changes to the rheology of ice samples can be found when rock particles are included in ice samples, and when H_2O is replaced by D_2O. Calculated parameters in an ice-rock flow law of the same form as that of Durham et al. [20] agree with previous literature results for dislocation creep [11,19], supported by observations of the deformation microstructure. However, the ice-rock flow law found here (Eq. 7) has a different value for the rock fraction exponent "b" than found previously. The reason for this difference may be due to external or internal experimental variables, and in order to extrapolate measured flow to natural processes, it is important in future investigations that these effects be constrained to determine the most accurate flow law parameters possible. An accurate grain-size-sensitive flow law is particularly important, as this is likely to be important at strain-rates found in a large range of environments [11]. Here we are able to suggest that the presence of rock has a similar effect on deformation at GSS conditions, as seen in the dislocation creep regime, but more data is required to confirm this. The mechanism of the increase in strength due to increasing rock particle content is not yet clear. It is possible to suggest that in some of the samples, sub-grain development and grain boundary movement is associated with the position of fluorite particles, which may be a result of pinned dislocations moving during deformation.

The findings here that D_2O replacement has an important effect on the deformation are of interest for neutron beam line experiments where deuterated samples are often used in place of hydrogenated materials. It is important to consider what effect this replacement has on the properties that are obtained, and note that H_2O and D_2O samples are not necessarily immediately comparable, even when compensating for the different temperature of freezing.

Although we have successfully developed sample preparation and experimental techniques, future work should be carried out to increase the amount of data available with a range of rock fractions, rock compositions, grain sizes, particle shape, and ratios of rock particle size to ice grain size, at a range of pressures, temperatures and strain-rates, allowing further investigation of the flow law. The factor of 2 increase in viscosity demonstrated here by the addition of rock particles shows that these flow laws should then be taken into account when considering simulation of processes, as results are likely to differ from results in a pure ice case.

Additional Information

Acknowledgments

We thank I. Wood, A. D. Fortes, S. Hunt, J. Bowles, S. Boon and J. Davy for fruitful discussions and assistance with experiments.

Funding Statement

C. A. Middleton was funded through a Science and Technology Facilities Council Ph.D studentship during this work. P. M. Grindrod was funded by STFC and UK Space Agency fellowships (grants ST/F011830/1, ST/J002127/1, ST/J005215/1, ST/L00254X).

Competing Interests

We have no competing interests.

Authors' Contributions

C. A. Middleton carried out the experiments, analysed and interpreted data and drafted the article. P. M. Grindrod and P. R. Sammonds provided substantial assistance with conception and execution of the experiments, data analysis and interpretation, and provided critical revisions of the article.

References

1. Arenson, L. U., Springman, S. M. & Sego, D. C. 2007 The Rheology of Frozen Soils. *Appl. Rheol.* **17**, 12147–1 – 12147–14. (doi:10.3933/ApplRheol-17-12147)
2. Durham, W. B., Pathare, A. V., Stern, L. A. & Lenferink, H. J. 2009 Mobility of icy sand packs, with application to Martian permafrost. *Geophys. Res. Lett.* **36**, L23203. (doi:10.1029/2009GL040392)
3. Mangold, N., Allemand, P., Duval, P., Geraud, Y. & Thomas, P. 2002 Experimental and theoretical deformation of ice–rock mixtures: Implications on rheology and ice content of Martian permafrost. *Planet. Space Sci.* **50**, 385–401. (doi:10.1016/S0032-0633(02)00005-3)
4. Hooke, R. L., Dahlin, B. B. & Kauper, M. T. 1972 Creep of ice containing dispersed fine sand. *J. Glaciol.* **11**, 327–336.
5. Echelmeyer, K. & Zhongxiang, W. 1987 Direct observation of basal sliding and deformation of basal drift at sub-freezing temperatures. *J. Glaciol.* **33**, 83–98.
6. Schulson, E. M. & Duval, P. 2009 *Creep and fracture of ice*. Cambridge University Press.
7. Schubert, G., Anderson, J. D., Spohn, T. & McKinnon, W. B. 2004 Interior composition, structure and dynamics of the Galilean satellites. In *Jupiter: The Planet, Satellites and Magnetosphere.* (eds F. Bagenal. T. E. Dowling & W. B. McKinnon), Cambridge University Press.
8. Anderson, J. D., Lau, E. L., Sjogren, W. L., Schubert, G. & Moore, W. B. 1996 Gravitational constraints on the internal structure of Ganymede. *Nature* **384**, 541–543. (doi:10.1038/384541a0)
9. Moore, P. L. 2014 Deformation of Debris-Ice Mixtures. *Rev. Geophys.* **52**, 435–467. (doi:10.1002/2014RG000453.Received)

10. Grindrod, P., Fortes, A., Nimmo, F., Feltham, D., Brodholt, J. & Vocadlo, L. 2008 The long-term stability of a possible aqueous ammonium sulfate ocean inside Titan. *Icarus* **197**, 137–151. (doi:10.1016/j.icarus.2008.04.006)
11. Durham, W. B. & Stern, L. A. 2001 Rheological properties of water ice - applications to satellites of the outer planets. *Annu. Rev. Earth Planet. Sci.* **29**, 295–330. (doi:10.1146/annurev.earth.29.1.295)
12. Goldsby, D. L. & Kohlstedt, D. L. 1997 Grain boundary sliding in fine-grained Ice I. *Scr. Mater.* **37**, 1399–1406. (doi:10.1016/S1359-6462(97)00246-7)
13. Goldsby, D. L. & Kohlstedt, D. L. 2001 Superplastic deformation of ice: Experimental observations. *J. Geophys. Res.* **106**, 11017. (doi:10.1029/2000JB900336)
14. Parameswaran, V. R. & Jones, S. J. 1981 Triaxial testing of frozen sand. *J. Glaciol.* **27**, 147–155.
15. Zhu, Y. L. & Carbee, D. L. 1984 Uniaxial compressive strength of frozen silt under constant deformation rates. *Cold Reg. Sci. Technol.* **9**, 3–15. (doi:10.1016/0165-232X(84)90043-0)
16. Domaschuk, L., Shields, D. H. & Rahman, M. 1991 A model for attenuating creep of frozen sand. *Cold Reg. Sci. Technol.* **19**, 145–161. (doi:10.1016/0165-232X(91)90005-2)
17. Arenson, L. U., Johansen, M. M. & Springman, S. M. 2004 Effects of volumetric ice content and strain rate on shear strength under triaxial conditions for frozen soil samples. *Permafr. Periglac. Process.* **15**, 261–271. (doi:10.1002/ppp.498)
18. Arenson, L. U. & Springman, S. M. 2005 Mathematical descriptions for the behaviour of ice-rich frozen soils at temperatures close to 0 ° C. *Can. Geotech. J.* **42**, 431–442. (doi:10.1139/T04-109)
19. Yang, Y., Lai, Y. & Li, J. 2010 Laboratory investigation on the strength characteristic of frozen sand considering effect of confining pressure. *Cold Reg. Sci. Technol.* **60**, 245–250. (doi:10.1016/j.coldregions.2009.11.003)
20. Yasui, M. & Arakawa, M. 2008 Experimental study on the rate dependent strength of ice-silica mixture with silica volume fractions up to 0.63. *Geophys. Res. Lett.* **35**, L12206. (doi:10.1029/2008GL033787)
21. Durham, W. B., Kirby, S. H. & Stern, L. A. 1992 Effects of Dispersed Particulates on the Rheology of Water Ice at Planetary Conditions. *J. Geophys. Res.* **97**, 20883–20897. (doi:10.1029/92JE02326)
22. Durham, W. B., Kirby, S. H. & Stern, L. A. 1997 Creep of water ices at planetary conditions : A compilation. *J. Geophys. Res.* **102**, 16293–16302.
23. Bennett, K., Wenk, H. R., Durham, W. B., Stern, L. A. & Kirby, S. H. 1997 Preferred crystallographic orientation in the ice I > II transformation and the flow of ice II. *Philos. Mag.* **A76**, 413–435. (doi:10.1080/01418619708209983)
24. McDaniel, S., Bennett, K., Durham, W. B. & Waddington, E. D. 2006 In situ deformation apparatus for time-of-flight neutron diffraction: Texture development of polycrystalline ice Ih. *Rev. Sci. Instrum.* **77**, 093902. (doi:10.1063/1.2349603)
25. Piazolo, S., Wilson, C. J. L., Luzin, V., Brouzet, C. & Peternell, M. 2013 Dynamics of ice mass deformation: Linking processes to rheology, texture, and microstructure. *Geochemistry, Geophys. Geosystems* **14**, 4185–4194. (doi:10.1002/ggge.20246)
26. Wilson, C. J. L., Peternell, M., Piazolo, S. & Luzin, V. 2014 Microstructure and fabric development in ice: Lessons learned from in situ experiments and implications for understanding rock evolution. *J. Struct. Geol.* **61**, 50–77. (doi:10.1016/j.jsg.2013.05.006)
27. Wilson, C. J. L., Luzin, V., Piazolo, S., Peternell, M. & Hammes, D. 2015 Experimental deformation of deuterated ice in 3D and 2D: Identification of grain-scale processes. *Proc. R. Soc. Victoria* **127**, 99–104. (doi:10.1071/RS15011)
28. Hobbs, P. V. 1974 *Ice Physics*. Oxford University Press.
29. Finney, J. L. 1995 The complementary use of X-ray and neutron diffraction in the study of crystals. *Acta Crystallogr. Sect. B Struct. Sci.* **51**, 447–467. (doi:10.1107/S0108768195002734)
30. Rist, M. A. 1989 The effect of temperature and strain rate on the triaxial deformation and strength of pure polycrystalline ice: an experimental study. PhD Thesis. University of London, London, U.K.
31. Cole, D. M. 1979 Preparation of polycrystalline ice specimens for laboratory experiments. *Cold Reg. Sci. Technol.* **1**, 153–159. (doi:10.1016/0165-232X(79)90007-7)
32. Jacka, T. H. 1984 Laboratory studies on relationships between ice crystal size and flow rate. *Cold Reg. Sci. Technol.* **10**, 31–42. (doi:10.1016/0165-232X(84)90031-4)
33. Poirier, J. P. 1985 *Creep of crystals: High-temperature deformation processes in metal, ceramics and minerals.* Cambridge University Press.
34. Jones, S. J. & Chew, H. A. M. 1981 On the grain-size dependence of secondary creep. *J. Glaciol.* **27**, 517–518.
35. Bloomfield, J. P. & Covey-Crump, S. J. 1993 Correlating mechanical data with microstructural observations in deformation experiments on synthetic two-phase aggregates. *J. Struct. Geol.* **15**, 1007–1019. (doi:10.1016/0191-8141(93)90173-8)
36. Mori, Y., Hondoh, T. & Higashi, A. 1985 Development of an automatic ice fabric analyser. *Ann. Glaciol.* **6**,

281–283.
37. Petrenko, V. F. & Whitworth, R. W. 1999 *Physics of Ice*. Oxford University Press.
38. Middleton, C. A. 2012 Investigation of the rheological properties of planetary ice-rock analogues using triaxial deformation and neutron diffraction experiments. PhD Thesis. University College London, London, U.K.
39. Huffman, D. R. & Norwood, M. H. 1960 Specific Heat and Elastic Constants of Calcium Fluoride at Low Temperatures. *Phys. Rev.* **117**, 709–711. (doi:10.1103/PhysRev.117.709)
40. Röttger, K., Endriss, A., Ihringer, J., Doyle, S. & Kuhs, W. F. 1994 Lattice constants and thermal expansion of H_2O and D_2O ice I h between 10 and 265 K. *Acta Crystallogr. Sect. B Struct. Sci.* **50**, 644–648. (doi:10.1107/S0108768194004933)
41. Sammonds, P. R. 1988 Triaxial deformation experiments on natural sea ice as a function of temperature and strain rate. PhD Thesis. University of London, London, U.K.
42. Sammonds, P. R., Murrell, S. A. F., Rist, M. A. & Butler, D. 1991 The design of a high-pressure low-temperature triaxial deformation cell for ice. *Cold Reg. Sci. Technol.* **19**, 177–188. (doi:10.1016/0165-232X(91)90007-4)
43. Rist, M. A., Sammonds, P. R. & Murrell, S. A. F. 1991 Strain rate control during deformation of ice: An assessment of the performance of a new servo-controlled triaxial testing system. *Cold Reg. Sci. Technol.* **19**, 189–200. (doi:10.1016/0165-232X(91)90008-5)
44. Raistrick, D. C. 1995 Flow of Greenland ice as a function of climatically determined ice characteristics, flow history and conditions at depth; studied by laboratory experiments on GRIP ice samples.
45. Kipfstuhl, S., Hamann, I., Lambrecht, A., Freitag, J., Faria, S. H., Grigoriev, D. & Azuma, N. 2006 Microstructure mapping: a new method for imaging deformation-induced microstructural features of ice on the grain scale. *J. Glaciol.* **52**, 398–406. (doi:10.3189/172756506781828647)
46. Higuchi, K. 1958 The etching of ice crystals. *Acta Metall.* **6**, 636–642. (doi:10.1016/0001-6160(58)90157-3)
47. Berger, A., Herwegh, M., Schwarz, J. O. & Putlitz, B. 2011 Quantitative analysis of crystal/grain sizes and their distributions in 2D and 3D. *J. Struct. Geol.* **33**, 1751–1763. (doi:10.1016/j.jsg.2011.07.002)
48. Faria, S. H., Freitag, J. & Kipfstuhl, S. 2010 Polar ice structure and the integrity of ice-core paleoclimate records. *Quat. Sci. Rev.* **29**, 338–351. (doi:10.1016/j.quascirev.2009.10.016)
49. Kipfstuhl, S., Faria, S. H., Azuma, N., Freitag, J., Hamann, I., Kaufmann, P., Miller, H., Weiler, K. & Wilhelms, F. 2009 Evidence of dynamic recrystallization in polar firn. *J. Geophys. Res.* **114**, B05204. (doi:10.1029/2008JB005583)
50. Weikusat, I., De Winter, D. A. M., Pennock, G. M., Hayles, M., Schneijdenberg, C. T. W. M. & Drury, M. R. 2011 Cryogenic EBSD on ice: preserving a stable surface in a low pressure SEM. *J. Microsc.* **242**, 295–310. (doi:10.1111/j.1365-2818.2010.03471.x)
51. Hamann, I., Weikusat, C., Azuma, N. & Kipfstuhl, S. 2007 Evolution of ice crystal microstructure during creep experiments. *J. Glaciol.* **53**, 479–489. (doi:10.3189/002214307783258341)
52. Glen, J. W. 1955 The creep of polycrystalline ice. *Proc. R. Soc. A Math. Phys. Eng. Sci.* **228**, 519–538. (doi:10.1098/rspa.1955.0066)
53. Blenkinsop, T. 2000 *Deformation microstructures and mechanisms in minerals and rocks.* Kluwer Academic Publishers.
54. Frost, H. J. & Ashby, M. F. 1982 *Deformation mechanism maps: The plasticity and creep of metals and ceramics*. Pergamon Press.
55. Stern, L. A., Durham, W. B. & Kirby, S. H. 1997 Grain-size-weakening of H_2O ices I and II and associated anisotropic recrystallization. *J. Geophys. Res.* **102**, 5313–5325. (doi:10.1029/96jb03894)
56. Weertman, J. 1983 Creep deformation of ice. *Annu. Rev. Earth Planet. Sci.* **11**, 215–240. (doi:10.1146/annurev.ea.11.050183.001243)
57. Barnes, P., Tabor, D. & Walker, J. C. F. 1971 The friction and creep of polycrystalline ice. *Proc. R. Soc. A Math. Phys. Eng. Sci.* **324**, 127–155. (doi:10.1098/rspa.1971.0132)
58. Goodman, D. J., Frost, H. J. & Ashby, M. F. 1981 The plasticity of polycrystalline ice. *Philos. Mag. A* , 665–695. (doi:10.1080/01418618108240401)

Figure and table captions

Table 1

Sample details, experimental conditions and results for pure ice, H_2O-ice-rock and D_2O-ice-rock samples of 10, 25 and 50 vol.% rock. $\varphi_{porosity}$ = volume fraction porosity (void space), assumed to be 2 % for ice-rock samples based on pure ice measurements; φ_{rock} = volume fraction rock; T = temperature; P = confining pressure; $\dot{\varepsilon}$ = imposed strain-rate; σ = measured steady state stress. Errors on stresses are 1 s.d.

Figure 1
Microstructural observations of pre-deformation pure ice (a-c) and ice-rock (d-f) samples. Thin section image in reflected light (a) shows a hexagonal texture with ice grains of similar sizes and smaller pores (void spaces) concentrated at grain boundary intersections. Scanning Electron Microscopy (SEM) images (b, c) also show this hexagonal structure, and quasi-linear grooves due to sublimation etching, which manifest in different directions in adjacent grains, indicated by arrows perpendicular to the texture in (c). Thin section image of 10 vol.% rock sample (d) shows similar hexagonal ice grains to those seen in pure ice samples, surrounding angular fluorite particles of a similar size. (e) SEM image of unknown rock fraction, the form of etch pits (circled) in the ice grains show that grains are oriented in different directions. (f) SEM image of 50 vol.% rock sample. Fluorite particles are seen in an ice matrix with no ice grain boundaries visible. Vertical lines visible in Fig (a) are due to irregularities in the microtome blade used for thinning and polishing the section. Fluorite particles colourised in post-processing.

Figure 2
Individual differential stress (blue) and strain (red) against time for the deformation run on sample H_2O+50%CaF_2_C, with P = 48 MPa, T = 263 K. Nominal strain-rates were 5 x 10^{-6}, 1 x 10^{-5}, 5 x 10^{-5} s^{-1}, increases in strain-rate shown by change in background colour. Features in the curves marked: A – seal friction, B – hit point, C – transient creep, D – steady-state creep, E and F – ramps in strain-rate, G – possible strain-hardening in strain-rate ramp 2, H – strain-hardening in strain-rate 3, I – apparent load jump likely due to friction on the ram, and unlikely to have been experienced by the sample.

Figure 3
Measured steady-state stresses vs imposed strain-rate for H_2O-ice and ice-rock samples at a confining pressure of 48 MPa and temperature of 253 K. The measured differential stress increases with increased strain-rate. Differential stresses measured for 10 vol.% samples have similar values to pure ice, but for higher rock fractions the stress increases with rock fraction. For clarity, error bars are not shown.

Figure 4
Measured steady-state stresses vs imposed strain-rate and calculated flow laws for all H_2O-ice and H_2O-ice-rock samples at all conditions. (a) pure ice; (b) ice + 10 vol.% fluorite samples; (c) ice + 25 vol.% fluorite; (d) ice + 50 vol.% fluorite. As well as an increase of measured differential stress due to an increased strain-rate and higher rock fraction, the differential stress also increases with lower temperature and higher confining pressure. Higher strain-rate data shows a good fit to the calculated flow laws for T = 253 K, whereas lower strain-rate data for pure ice, 25 and 50 vol.% rock may be better described by a GSS regime represented by the n = 1.8 flow law. The temperature dependence of the flow law is well described for pure ice, but for 50 vol.% rock, the flow law underestimates the measured strengths. Lighter blue diamonds are lower bounds on steady-state stresses due to extended transient creep effect discussed in text. Errors on stresses are 1 s.d., flow law parameters are detailed in Table 2.

Figure 5
Measured steady-state stresses vs imposed strain-rate and calculated flow laws for all D_2O-ice-rock samples. Measured stress increases with strain-rate, lower temperature and increased rock fraction.

Figure 6
Post deformation microstructures of ice and ice-rock samples. (a) evidence of grain size changes due to recrystallization, and sub-grain development and grain boundary bulging in reflected light microscope image of a pure ice sample. (b) evidence of recrystallisation of ice in a 10 vol.% rock sample transmitted light image. (c) grain boundary migration and recrystallisation to grains with a more rectangular habit in a SEM image of a 10 vol.% rock sample. (d) grain boundary bulging and the possibility of grain boundary formation associated with rock particles in a SEM image of a 10 vol.% rock sample. (e) Development of a rectangular habit of ice grains, possibly associated with a rock particle, in a transmitted light thin section image of a 25 vol.% rock sample. (f) Impaction and fragmentation of rock particles in a SEM image of a 50 vol.% rock sample.

Table 2
Flow law parameters for the three flow law scenarios described in text. * values from [11].

Sample (deformation run in brackets)	Length (mm)	Diameter (mm)	Mass (g)	$\varphi_{porosity}$ (%)	φ_{rock} (%)	T (K)	P (MPa)	$\dot{\varepsilon}$ (s^{-1})	σ (MPa)
Pure ice									
H_2O+0%CaF_2_A (1)	65	24.75	28.14	1.87 ± 1.18	-	263 ± 1.5	47.5 ± 0.5	5.18×10^{-6}	2.93 ± 0.24
(2)						263 ± 1.5	47.5 ± 0.5	1.07×10^{-5}	3.46 ± 0.21
(3)						263 ± 1.5	47.5 ± 0.5	5.65×10^{-5}	4.39 ± 0.17
H_2O+0%CaF_2_B (1)	64.5	24.75	27.8	2.30 ± 1.18	-	263 ± 1.5	47.5 ± 0.5	1.52×10^{-6}	1.88 ± 0.25
(2)						263 ± 1.5	47.5 ± 0.5	2.62×10^{-6}	2.55 ± 0.24
(3)						263 ± 1.5	47.5 ± 0.5	5.40×10^{-6}	3.04 ± 0.22
H_2O+0%CaF_2 C (1)	65.2	24.7	28.27	1.00 ± 1.20	-	253 ± 1.5	47.5 ± 0.5	1.04×10^{-5}	5.73 ± 0.19
(2)						253 ± 1.5	47.5 ± 0.5	5.53×10^{-5}	7.30 ± 0.19
H_2O+0%CaF_2 D (1)	65.2	24.7	28.2	1.25 ± 1.19	-	253 ± 1.5	47.5 ± 0.5	9.33×10^{-7}	2.55 ± 0.45
(2)						253 ± 1.5	47.5 ± 0.5	2.47×10^{-6}	4.21 ± 0.21
(3)						253 ± 1.5	47.5 ± 0.5	5.22×10^{-6}	4.96 ± 0.23
(4)						253 ± 1.5	47.5 ± 0.5	1.07×10^{-5}	5.75 ± 0.20
(5)						253 ± 1.5	47.5 ± 0.5	2.75×10^{-5}	6.72 ± 0.19
(6)						253 ± 1.5	47.5 ± 0.5	5.73×10^{-5}	7.89 ± 0.22
H_2O-ice + 10 vol.% rock									
H_2O+10%CaF_2_A (1)	64.9	24.7	38.3	2	14.8 ± 0.28	253 ± 1.5	47.5 ± 0.5	1.04×10^{-5}	5.62 ± 0.20
(2)						253 ± 1.5	47.5 ± 0.5	5.53×10^{-5}	7.77 ± 0.21
H_2O+10%CaF_2_B (1)	64	24.6	32.4	2	7.4 ± 0.14	253 ± 1.5	47.5 ± 0.5	5.21×10^{-6}	4.79 ± 0.25
(2)						253 ± 1.5	47.5 ± 0.5	1.09×10^{-5}	5.43 ± 0.24
(3)						253 ± 1.5	47.5 ± 0.5	5.66×10^{-5}	7.80 ± 0.23
H_2O+10%CaF_2_C (1)	65.1	24.7	34.3	2	9.0 ± 0.17	253 ± 1.5	47.5 ± 0.5	2.52×10^{-6}	3.92 ± 0.23
(2)						253 ± 1.5	47.5 ± 0.5	5.25×10^{-6}	4.83 ± 0.22
(3)						253 ± 1.5	47.5 ± 0.5	1.09×10^{-5}	5.66 ± 0.22
(4)						253 ± 1.5	47.5 ± 0.5	2.80×10^{-5}	6.88 ± 0.22
(5)						253 ± 1.5	47.5 ± 0.5	5.80×10^{-5}	8.25 ± 0.23
H_2O+10%CaF_2_D (1)	65	24.5	34.9	2	10.6 ± 0.20	253 ± 1.5	47.5 ± 0.5	1.03×10^{-6}	3.98 ± 0.31
(2)						253 ± 1.5	47.5 ± 0.5	2.67×10^{-6}	4.95 ± 0.23
(3)						253 ± 1.5	47.5 ± 0.5	5.43×10^{-6}	5.62 ± 0.22
(4)						253 ± 1.5	47.5 ± 0.5	1.09×10^{-5}	6.39 ± 0.21
(5)						253 ± 1.5	47.5 ± 0.5	5.29×10^{-6}	5.18 ± 0.30
(6)						253 ± 1.5	47.5 ± 0.5	1.09×10^{-5}	6.09 ± 0.26
(7)						253 ± 1.5	47.5 ± 0.5	5.70×10^{-5}	8.94 ± 0.21
D_2O-ice + 10 vol.% rock									
D_2O+10%CaF_2_A (1)	65.5	25.1	38.8	2	9.2 ± 0.17	253 ± 1.5	48 ± 2	5.12×10^{-7}	3.70 ± 0.84
D_2O+10%CaF_2_B (1)	64.25	24.8	37.7	2	9.8 ± 0.18	253 ± 1.5	48 ± 2	2.51×10^{-6}	6.30 ± 0.31
(2)						253 ± 1.5	48 ± 2	5.40×10^{-6}	7.95 ± 1.19
(3)						233 ± 1.5	48 ± 2	5.52×10^{-6}	12.22 ± 0.83
D_2O+10%CaF_2_C (1)	62.5	24.1	37.4	2	14.5 ± 0.27	253 ± 1.5	47.5 ± 0.5	5.10×10^{-6}	9.25 ± 0.45
(2)						253 ± 1.5	47.5 ± 0.5	5.26×10^{-5}	15.85 ± 0.29
H_2O-ice + 25 vol.% rock									
H_2O+25%CaF_2_A	65.3	24.75	43.7	2	21.7 ± 0.40	*Not deformed*			
H_2O+25%CaF_2_B (1)	64.9	24.6	46.7	2	27.2 ± 0.51	253 ± 1.5	47.5 ± 0.5	1.02×10^{-6}	3.35 ± 0.36
(2)						253 ± 1.5	47.5 ± 0.5	2.62×10^{-6}	4.53 ± 0.30
(3)						253 ± 1.5	47.5 ± 0.5	5.34×10^{-6}	5.55 ± 0.26
(4)						253 ± 1.5	47.5 ± 0.5	1.08×10^{-5}	6.55 ± 0.28
(5)						253 ± 1.5	47.5 ± 0.5	2.82×10^{-5}	8.46 ± 0.29
(6)						253 ± 1.5	47.5 ± 0.5	5.87×10^{-5}	10.23 ± 0.25
D_2O-ice + 25 vol.% rock									
D_2O+25%CaF_2_A (1)	65	25	50.7	2	27.2 ± 0.50	253 ± 1.5	48 ± 2	1.48×10^{-6}	10.32 ± 0.39
(2)						253 ± 1.5	48 ± 2	5.47×10^{-6}	12.68 ± 0.85
D_2O+25%CaF_2_B (1)	61.4	24.5	49.2	2	32.3 ± 0.60	253 ± 1.5	47.5 ± 0.5	5.28×10^{-6}	8.57 ± 0.35
(2)						253 ± 1.5	47.5 ± 0.5	1.10×10^{-5}	9.88 ± 0.28
(3)						253 ± 1.5	47.5 ± 0.5	2.82×10^{-5}	11.72 ± 0.27
(4)						253 ± 1.5	47.5 ± 0.5	5.79×10^{-5}	14.06 ± 0.29
D_2O+25%CaF_2_C (1)	61.7	24	42.9	2	24.9 ± 0.49	*Loading failed*			
H_2O-ice + 50 vol.% rock									
H_2O+50%CaF_2_A (1)	65	25.25	68	2	51.7 ± 1.05	263 ± 1.5	0	5.10×10^{-6}	2.67 ± 0.17
H_2O+50%CaF_2_B (1)	65	25.25	66	2	49.0 ± 1.02	263 ± 1.5	0	5.59×10^{-6}	2.58 ± 0.50
(2)						263 ± 1.5	0	1.11×10^{-5}	3.18 ± 0.09
H_2O+50%CaF_2_C (1)	65.8	24.7	61.8	2	47.5 ± 1.03	263 ± 1.5	47.5 ± 0.5	5.12×10^{-6}	5.53 ± 0.21
(2)						263 ± 1.5	47.5 ± 0.5	1.06×10^{-5}	7.66 ± 0.21
(3)						263 ± 1.5	47.5 ± 0.5	5.63×10^{-5}	11.3 ± 0.30
H_2O+50%CaF_2_D (1)	64.8	24.75	62	2	47.2 ± 1.02	*Fractured in loading*			
H_2O+50%CaF_2_E (1)	65.25	24.6	61.6	2	47.2 ± 1.03	253 ± 1.5	47.5 ± 0.5	2.64×10^{-6}	7.28 ± 0.31
H_2O+50%CaF_2_F (1)	65.4	24.6	61.7	2	47.2 ± 1.03	253 ± 1.5	47.5 ± 0.5	8.59×10^{-7}	*2.38 ± 0.69*
(2)						253 ± 1.5	47.5 ± 0.5	2.59×10^{-6}	*5.40 ± 0.45*
(3)						253 ± 1.5	47.5 ± 0.5	5.38×10^{-6}	7.63 ± 0.40
(4)						253 ± 1.5	47.5 ± 0.5	1.13×10^{-5}	9.62 ± 0.31
H_2O+50%CaF_2_G (1)	64	24.5	60.5	2	48.0 ± 1.04	253 ± 1.5	47.5 ± 0.5	2.68×10^{-6}	*6.58 ± 0.37*
(2)						253 ± 1.5	47.5 ± 0.5	5.74×10^{-5}	15.24 ± 0.25
D_2O-ice + 50 vol.% rock									
D_2O+50%CaF_2_A (1)	62.5	24.1	60.3	2	50.7 ± 1.17	253 ± 1.5	47.5 ± 0.5	5.22×10^{-6}	*15.62 ± 0.37*
(2)						253 ± 1.5	47.5 ± 0.5	1.12×10^{-5}	19.54 ± 0.39
(3)						253 ± 1.5	47.5 ± 0.5	5.74×10^{-5}	26.48 ± 0.34

Table 1.

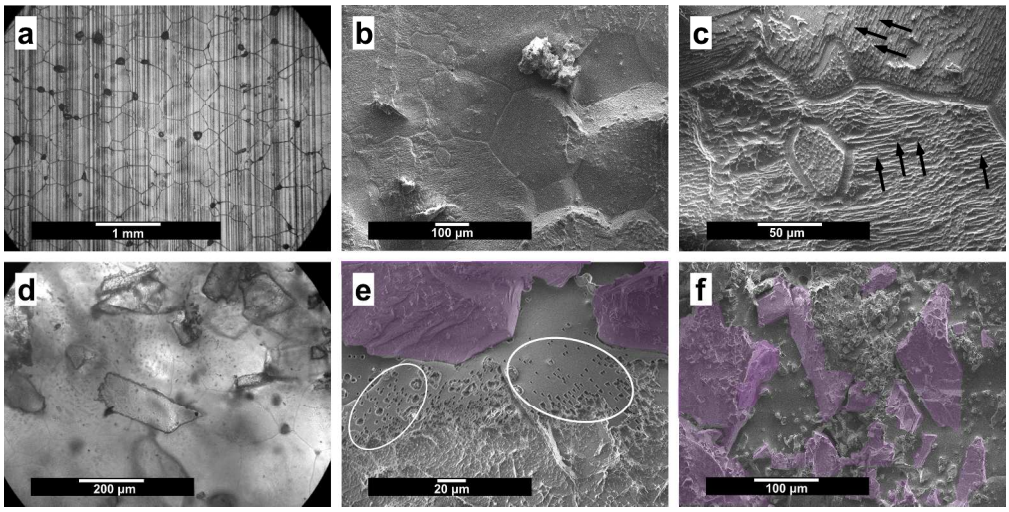

Microstructural observations of pre-deformation pure ice (a-c) and ice-rock (d-f) samples. Thin section image in reflected light (a) shows a hexagonal texture with ice grains of similar sizes and smaller pores (void spaces) concentrated at grain boundary intersections. Scanning Electron Microscopy (SEM) images (b, c) also show this hexagonal structure, and quasi-linear grooves due to sublimation etching, which manifest in different directions in adjacent grains, indicated by arrows perpendicular to the texture in (c). Thin section image of 10 vol.% rock sample (d) shows similar hexagonal ice grains to those seen in pure ice samples, surrounding angular fluorite particles of a similar size. (e) SEM image of unknown rock fraction, the form of etch pits (circled) in the ice grains show that grains are oriented in different directions. (f) SEM image of 50 vol.% rock sample. Fluorite particles are seen in an ice matrix with no ice grain boundaries visible. Vertical lines visible in Fig (a) are due to irregularities in the microtome blade used for thinning and polishing the section. Fluorite particles colourised in post-processing.

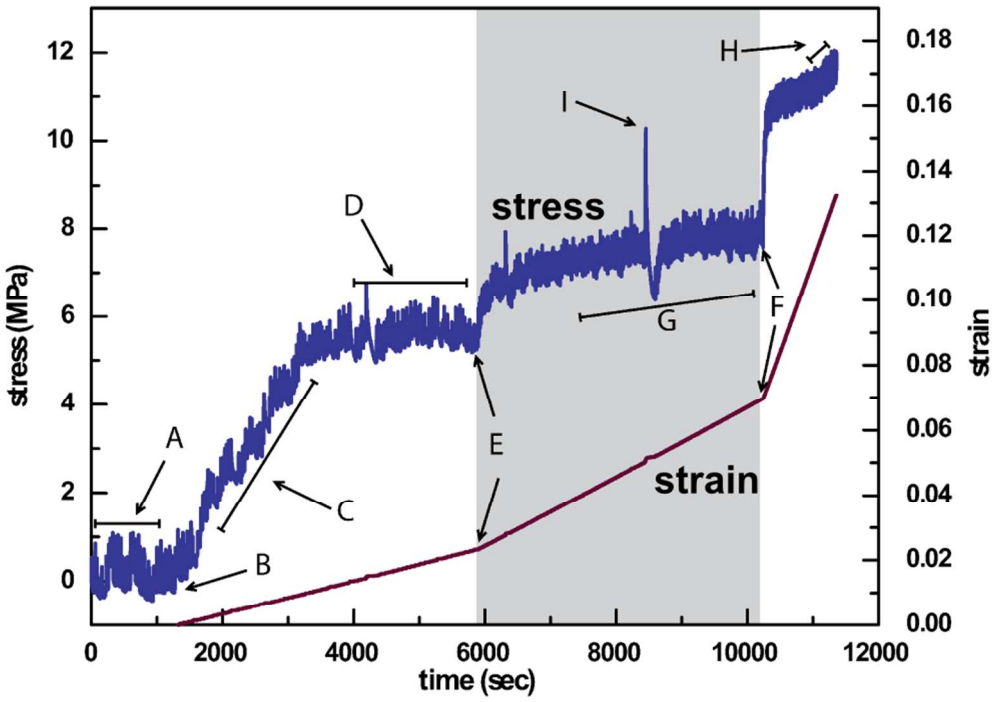

Individual differential stress (blue) and strain (red) against time for the deformation run on sample H_2O+50%CaF_2_C, with P = 48 MPa, T = 263 K. Nominal strain-rates were 5 x 10^{-6}, 1 x 10^{-5}, 5 x 10^{-5} s^{-1}, increases in strain-rate shown by change in background colour. Features in the curves marked: A – seal friction, B – hit point, C – transient creep, D – steady-state creep, E and F – ramps in strain-rate, G – possible strain-hardening in strain-rate ramp 2, H – strain-hardening in strain-rate 3, I – apparent load jump likely due to friction on the ram, and unlikely to have been experienced by the sample.

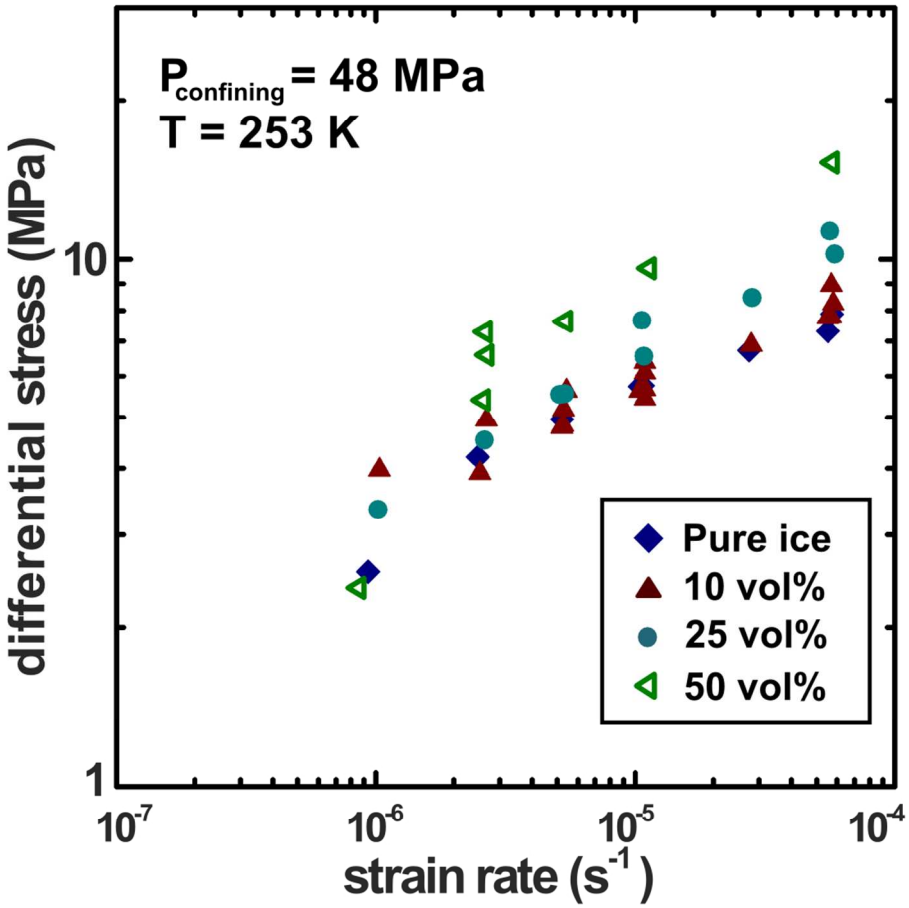

Measured steady-state stresses vs imposed strain-rate for H_2O-ice and ice-rock samples at a confining pressure of 48 MPa and temperature of 253 K. The measured differential stress increases with increased strain-rate. Differential stresses measured for 10 vol.% samples have similar values to pure ice, but for higher rock fractions the stress increases with rock fraction. For clarity, error bars are not shown.

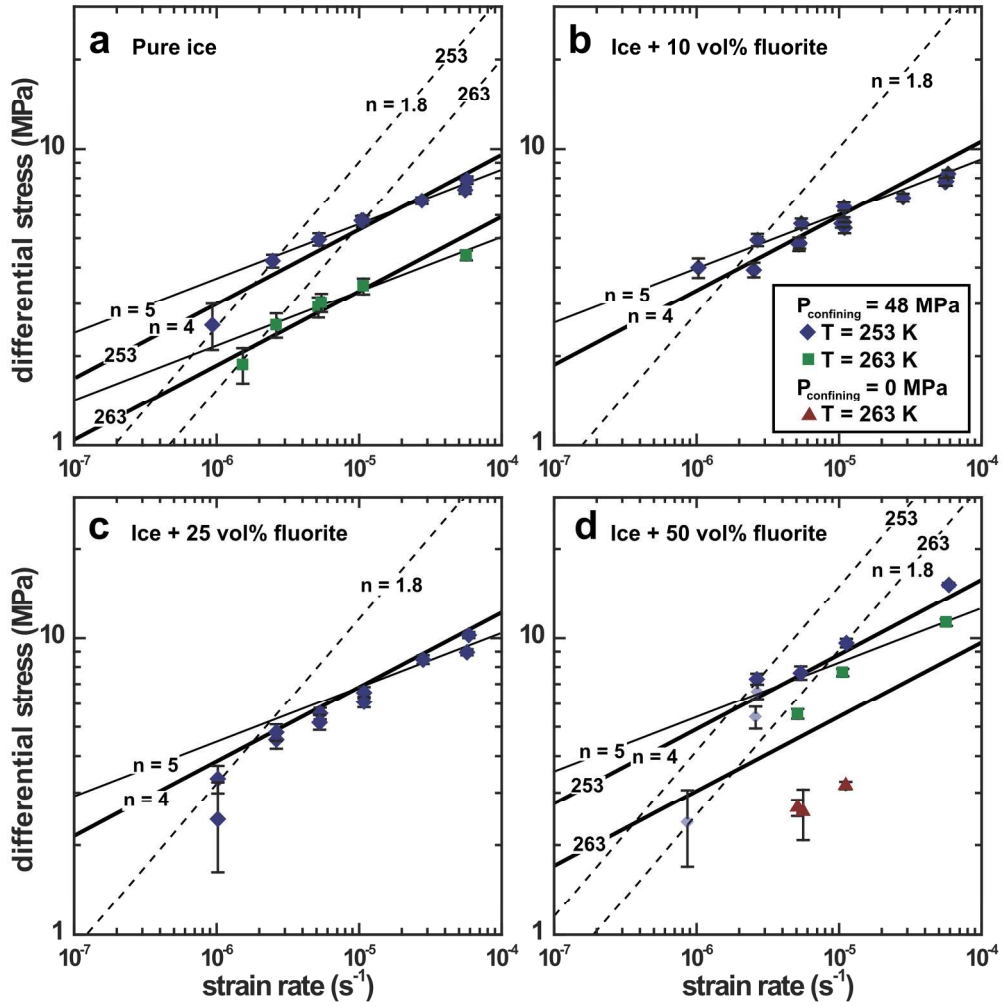

Measured steady-state stresses vs imposed strain-rate and calculated flow laws for all H_2O-ice and H_2O-ice-rock samples at all conditions. (a) pure ice; (b) ice + 10 vol.% fluorite samples; (c) ice + 25 vol.% fluorite; (d) ice + 50 vol.% fluorite. As well as an increase of measured differential stress due to an increased strain-rate and higher rock fraction, the differential stress also increases with lower temperature and higher confining pressure. Higher strain-rate data shows a good fit to the calculated flow laws for T = 253 K, whereas lower strain-rate data for pure ice, 25 and 50 vol.% rock may be better described by a GSS regime represented by the n = 1.8 flow law. The temperature dependence of the flow law is well described for pure ice, but for 50 vol.% rock, the flow law underestimates the measured strengths. Lighter blue diamonds are lower bounds on steady-state stresses due to extended transient creep effect discussed in text. Errors on stresses are 1 s.d., flow law parameters are detailed in Table 2.

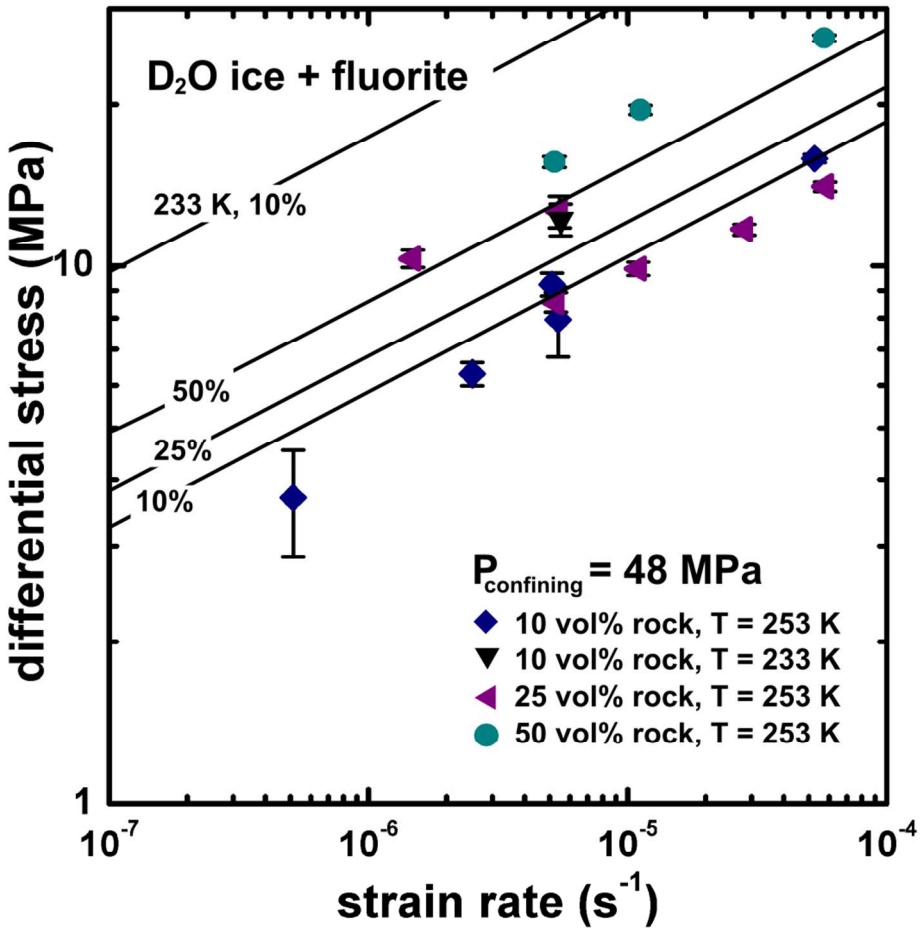

Measured steady-state stresses vs imposed strain-rate and calculated flow laws for all D_2O-ice-rock samples. Measured stress increases with strain-rate, lower temperature and increased rock fraction.

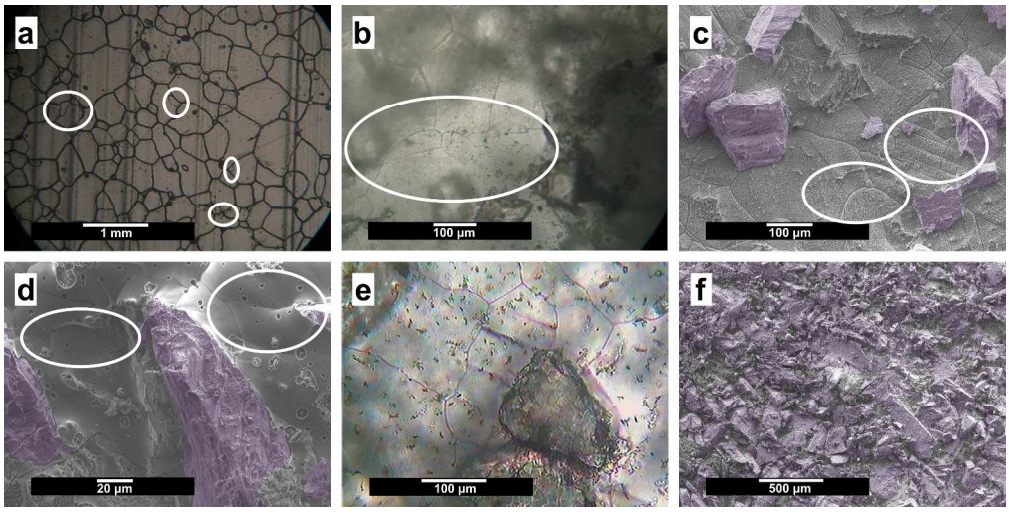

Post deformation microstructures of ice and ice-rock samples. (a) evidence of grain size changes due to recrystallization, and sub-grain development and grain boundary bulging in reflected light microscope image of a pure ice sample. (b) evidence of recrystallisation of ice in a 10 vol.% rock sample transmitted light image. (c) grain boundary migration and recrystallisation to grains with a more rectangular habit in a SEM image of a 10 vol.% rock sample. (d) grain boundary bulging and the possibility of grain boundary formation associated with rock particles in a SEM image of a 10 vol.% rock sample. (e) Development of a rectangular habit of ice grains, possibly associated with a rock particle, in a transmitted light thin section image of a 25 vol.% rock sample. (f) Impaction and fragmentation of rock particles in a SEM image of a 50 vol.% rock sample.

Table 2

Parameter	All data	High strain-rate	Low strain-rate
A	$1.02 \times 10^{14} \pm 1.00 \times 10^{13}$	$1.71 \times 10^{23} \pm 7.03 \times 10^{21}$	$1.65 \times 10^{-2} \pm 5.94 \times 10^{-4}$
Q (kJ mol^{-1})	106.1 ± 16.5	156.44 ± 9.4	49*
b	1.00 ± 0.06	0.83 ± 0.08	1
n	3.98 ± 0.35	5.45 ± 0.23	1.8*
p	-	-	1.4*